



Article

# Multifractal Detrended Fluctuation Analysis of Temperature Reanalysis Data over Greece

Kostas Philippopoulos <sup>1</sup>, Nikolaos Kalamaras <sup>1,2</sup>, Chris G. Tzanis <sup>1,\*</sup>, Despina Deligiorgi <sup>1</sup> and Ioannis Koutsogiannis <sup>1</sup>

<sup>1</sup> Section of Environmental Physics and Meteorology, Department of Physics, National and Kapodistrian University of Athens, 15784 Athens, Greece; kostasphilippopoulos@yahoo.com (K.P.); nikalamaras1@gmail.com (N.K.); despo@phys.uoa.gr (D.D.); koutsog@phys.uoa.gr (I.K.)

<sup>2</sup> Department of Weather Stations, Hellenic National Meteorological Service (HNMS), 16777 Athens, Greece

\* Correspondence: chtzanis@phys.uoa.gr

Received: 21 May 2019; Accepted: 13 June 2019; Published: 20 June 2019



**Abstract:** The Multifractal Detrended Fluctuation Analysis (MF-DFA) is used to examine the scaling behavior and the multifractal characteristics of the mean daily temperature time series of the ERA-Interim reanalysis data for a domain centered over Greece. The results showed that the time series from all grid points exhibit the same behavior: they have a positive long-term correlation and their multifractal structure is insensitive to local fluctuations with a large magnitude. Special emphasis was given to the spatial distribution of the main characteristics of the multifractal spectrum: the value of the Hölder exponent, the spectral width, the asymmetry, and the truncation type of the spectra. The most interesting finding is that the spatial distribution of almost all spectral parameters is decisively determined by the land–sea distribution. The results could be useful in climate research for examining the reproducibility of the nonlinear dynamics of reanalysis datasets and model outputs.

**Keywords:** air temperature; nonlinear dynamics; Multifractal Detrended Fluctuation Analysis; reanalysis data

## 1. Introduction

Many processes in nature are governed by nonlinear laws and they can be considered to be nonlinear systems that are described by nonlinear differential equations. A nonlinear system can be described effectively by the time series of a characteristic set of the system's parameters. A noticeable characteristic of many time series that result from nonlinear systems is the self-similarity, where, when part of the time series is enlarged, it is exactly the same as, or approximately similar to, the whole time series. Self-similarity is a very important feature of fractal time series and it is apparent in many scales of time and magnitude. In nature, there are many time series with a fractal structure and, ever since the primary studies of Benoit B. Mandelbrot [1,2], a great number of studies and books about fractals have been published [3–5].

Nonlinear systems' time series often exhibit a complex behavior that poses significant difficulties for their study using conventional linear methods, such as autocorrelation function analysis or spectral analysis. The presence of non-stationarities makes these methods totally unreliable for the detection of such time series properties [6]. On the other hand, the Detrended Fluctuation Analysis (DFA), introduced by Peng et al. [7], is a reliable method for finding the scaling properties of time series and detecting long-range correlations even in time series that appear to be non-stationary [8]. Scientists from various disciplines have exploited the advantages of DFA in their respective disciplines, such as financial market analysis [9,10], medical time series [11], DNA sequences [12], and natural and social phenomena [13–15]. Atmospheric processes interact in a complex way and obey nonlinear

laws [16]. Thus, meteorological parameter records (e.g., temperature, humidity, precipitation, wind speed) exhibit a fractal structure and their fractal scaling behavior can be studied using the DFA method. A great number of studies have applied DFA successfully to meteorological time series. More specifically, DFA has been used in the study of climate for temperature time series [17–22], relative humidity [23,24], precipitation amount [25], drought and flood indices [26], ozone data [27–30], incident flux of solar radiation [31], examining the variability of the atmosphere for a very wide temporal range [32], and the North Atlantic Oscillation [33], among others.

A basic prerequisite for the application of the DFA method is that there is a single scaling exponent for all scales (i.e., monofractal time series). However, in nature, very often time series have a fractal structure that demands a multitude of scaling exponents for different scales in order to be described completely. These time series are called ‘multifractal’, and they can be analyzed using a generalization of the DFA method—the multifractal DFA (MF-DFA)—that was introduced by Kandelhardt et al. [34]. A thorough presentation of multifractal statistics and an application of nonlinear dynamics to weather and climate is presented by Lovejoy and Schertzer [35]. In general, meteorological time series have a multifractal structure and the MF-DFA has been used for the analysis of temperature time series [36], precipitation amount data [37–39], wind speed records [40–42], climate studies [43,44], agrometeorological data [45,46], particulate matter data [47], and paleoclimatic records [48], among others.

Following the findings of Kalamaras et al. [49], which are based on observational temperature records over Greece, the scope of this study is to examine the behavior and the spatial distribution of multifractal spectrum characteristics using temperature time series from a reanalysis dataset. In the following section, the characteristics of the area under study are presented along with the extracted subset of the temperature time series from the ERA-Interim dataset. In the methodology section, there is a detailed reference for the main multifractal spectrum features. In the results and discussion sections, the resulting multifractal spectra are examined in association with climatic features and compared with the principal results presented in [49].

## 2. Area of Study and Data

The area under study is Greece, which is located at the southern part of the Balkans in southeast Europe. Despite the fact that it covers a relatively small geographic area, it exhibits a significant climatic variability [50] due to its complex topography and its location. This is clearly demonstrated by Karras [51], who applied the Thornwaite method of climatic classification in Greece and found 29 distinct climate regions. A characteristic example of this climate variety is the remarkable climatic difference between the northwestern Greek regions and the southeast insular parts of Greece as is clearly illustrated in the Hellenic National Meteorological Service (HNMS) climate atlas. These climatic differences may be identified by the analysis of temperature time series over Greece [52]. Therefore, there is an increased interest in the spatial distribution of the multifractal properties of meteorological time series from different parts of Greece.

The daily temperature time series in this study were extracted from the ERA-Interim reanalysis dataset of the European Centre for Medium-Range Weather Forecasts (ECMWF). It should be noted that the mean daily 2 m temperature data values were calculated as the mean value of the four available synoptic hours per day (00, 06, 12, and 18 UTC). The covered area is 34.50° N–42.00° N and 18.75° E–28.50° E using a 0.75° × 0.75° grid, and the relevant points are illustrated in Figure 1. Therefore, 154 (11 × 14) grid points were used, that cover uniformly the Greek area for a 35-year period (January 1979 to December 2014). The 2 m temperature values of the ERA-Interim dataset were estimated using not only surface temperature observations but also other data sources, mainly satellite observations. From the assimilation of the observations, ERA Interim produces four analyses per day at 00, 06, 12, and 18 UTC. Therefore, there are four temperature values per day and per grid point and, in this study, each daily temperature value is the average of these four values for each grid point. Moreover, each temperature value encompasses observations before and after the specified observation time,

i.e., for the production of the 00 UTC analysis, observations taken between 15 UTC on the previous day and 03 UTC on the present day were used and, similarly, observations taken between 03 and 15 UTC were used for the analysis of 12 UTC. The use of temperature data from reanalysis datasets has additional advantages related to data completeness and the quality control of the time series. A complete description of the ECMWF ERA-Interim dataset can be found in [53] and [54].

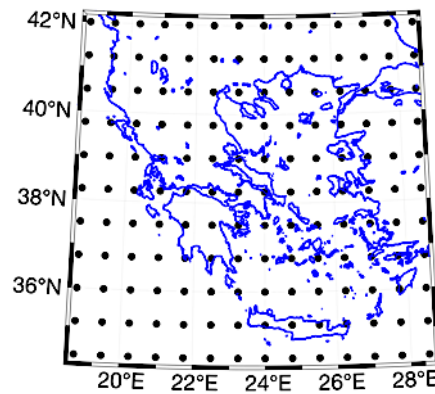


Figure 1. The area of study and the ERA-Interim reanalysis grid points.

### 3. Methods

This study consists of two parts:

- In the first part, the multifractal characteristics of reanalysis daily temperature are studied using MF-DFA;
- In the second part, the spatial distribution of the main multifractal spectral characteristics is examined.

The MF-DFA is used to study the scaling properties of the temperature time series. A brief description of the method is given below, while a more detailed description is elaborated in [34].

- Initially, the time series are deseasonalized by subtracting the mean value of each calendar day from the corresponding values of the time series. For instance, in a daily temperature time series covering the period 1979–2014, the deseasonalized value of temperature on a specific date is calculated by subtracting the mean value of this day of all years (i.e., the mean from 36 values).
- Subsequently, the ‘profile’  $Y(i)$  of the deseasonalized time series  $x_k$  of length  $N$  is found:

$$Y(i) \equiv \sum_{k=1}^i [x_k - \langle x \rangle] \tag{1}$$

where  $\langle x \rangle$  is the mean of the time series and  $i = 1, \dots, N$ .

- $Y(i)$  is then divided into  $N_s = \text{int}(N/s)$  boxes of equal length  $s$  ( $s$  being the time scale).
- In each box of length  $s$ , a least squares line is fitted to the data, which represents the trend in that box; i.e., the local trend. By subtracting the local trends,  $Y(i)$  is detrended and thus the variance  $F^2(v, s)$  of each segment (box) ( $v = 1, \dots, 2N_s$ ) is calculated. In this study, second-order trends were eliminated from the profile  $Y(i)$  using quadratic polynomials and, according to [34], linear trends were removed from the original time series.
- In order to find the  $q$ th order fluctuation function, the average overall segments are calculated:

$$F_q(s) = \left\{ \frac{1}{2N_s} \sum_{v=1}^{2N_s} [F^2(v, s)]^{\frac{q}{2}} \right\}^{\frac{1}{q}} \sim s^{h(q)}. \tag{2}$$

Equation (2) is valid when  $q \neq 0$ . If  $q = 0$ , the value of  $F_0(s)$  is found using Equation (3):

$$F_0(s) = \exp \left\{ \frac{1}{4N_s} \sum_{v=1}^{2N_s} \ln [F^2(v, s)] \right\} \sim s^{h(0)}. \tag{3}$$

- This quantity is calculated repeatedly for all time scales to determine the relationship between  $F_q(s)$  and  $s$ . Typically,  $F_q(s)$  is an increasing function of  $s$ .

The exponent  $h(q)$  usually depends on  $q$ . If  $q = 2$ , then, for stationary time series,  $h(2)$  is the Hurst exponent  $H$ . If the time series is monofractal, then  $h$  is independent of  $q$ . In the case of a different scaling between small and large fluctuations, significant dependencies are observed.

Disregarding for a moment the dependency of the Hurst exponent on  $q$  and assuming that  $h(q) = H$ , it is important to note that the time series is long-range anticorrelated for  $0 < H < 0.5$ ; uncorrelated for  $H = 0.5$ ; and long-range positively correlated for  $H > 0.5$ . Furthermore, if:

$$\begin{aligned} \tau(q) &= qh(q) - 1, \\ \text{then } \tau'(q) &= \alpha \\ \text{and } f(\alpha) &= q\alpha - \tau(q) = q[\alpha - h(q)] + 1. \end{aligned} \tag{4}$$

The quantity  $\alpha$  is called *singularity strength* (or the Hölder exponent) and  $f(\alpha)$  expresses the dimension of the subset of the time series that is characterized by  $\alpha$ . The plot of  $\alpha$  versus  $f(\alpha)$  is called a *singularity spectrum* (or *multifractal spectrum*). The value of  $\alpha$  where  $f(\alpha)$  takes its maximum value is when  $df(\alpha)/d\alpha = 0$ , satisfied when  $q = 0$ . From (4), it is found that  $f(\alpha)_{max} = 1$ . This value of  $\alpha$  corresponds to the most dominant scaling behavior [55] and it is the dominant Hurst exponent. Hereafter, this quantity will be denoted by  $\alpha_0$ . Another important feature of the spectrum is its *width* ( $\alpha_{max} - \alpha_{min}$ ), where  $\alpha_{max}$  and  $\alpha_{min}$  are the maximum and the minimum values of  $\alpha$  for which  $f(\alpha) = 0$ , which is a multifractality measure. A spectrum with a broad width has a strong multifractality (i.e., it has a ‘fine’ structure). If the width decreases, then the multifractality becomes weaker and the time series tends to be a monofractal one. The spectrum width of a pure monofractal time series is equal to zero. More details about the multifractal spectrum can be found in [56]. As recommended by Shimizu et al. [57], a measure of the width of the multifractal spectrum can be obtained by fitting a second-order equation to the curve of the spectrum around  $\alpha_0$ , according to:

$$G(a) = A(a - a_0)^2 + B(a - a_0) + C \tag{5}$$

where  $B$  is an asymmetry parameter. For  $B = 0$ , the spectrum is symmetrical; for  $B > 0$ , the spectrum is right-skewed; and, for negative  $B$  values, the spectrum is left-skewed [58]. A right-skewed spectrum is related to relatively strongly weighted high fractal exponents, whereas a left-skewed spectrum is indicative of low fractal exponents (a more ‘regular’ time series). According to [57], a time series with a high value of  $\alpha_0$ , a broad width, and a right-skewed spectrum is considered to be more ‘complex’ than a time series with the opposite characteristics.

Since the range of  $q$  values for which the spectrum is plotted is finite, it is very often observed that the spectrum is not symmetrical, and one of its legs is truncated. Therefore, the shape of the multifractal spectrum can be also characterized by its truncation type. The shape of the spectrum can be symmetrical, left truncated, or right truncated. According to [49], the truncation type is grouped into four categories: LL (a high degree of truncation on the left side, i.e., when the left side of the spectrum is shorter than the half of the length of the right side); L (left-truncated, when the left side of the spectrum is shorter (but not less than half) than the right side); S (symmetrical, when left side has almost equal length to the right side); and R (right-truncated, when the right side is shorter than the left side). The distinction between L and LL was made because it was found that most of the spectra are left-truncated, and this can be a convenient way to better study their asymmetry.

According to [34], multifractality is due to either a broad probability density function of the time series values, or to different long-range correlations for fluctuations of large and small magnitude. In order to examine this, the time series values were ordered randomly (shuffling) and MF-DFA was applied to the shuffled time series. If multifractal characteristics are preserved, then multifractality is caused by a broad probability density function. If not, the multifractality is due to different long-range correlations for different magnitudes of the time series fluctuations.

### 4. Results

#### 4.1. Multifractal Characteristics

The application of the MF-DFA to the daily temperature for each grid point (154 time series), yields to the plots of the fluctuation factor  $F_q(s)$  versus times scale  $s$ , the generalized Hurst exponent  $h(q)$  versus  $q$ , and the multifractal spectrum  $f(\alpha)$  versus  $\alpha$ . In Figures 2 and 3, these plots are presented along with the original and deseasonalized time series for the closest grid point to Athens (38.25° N, 24.00° E) and Kastoria (40.50° N, 21.00° E), respectively.

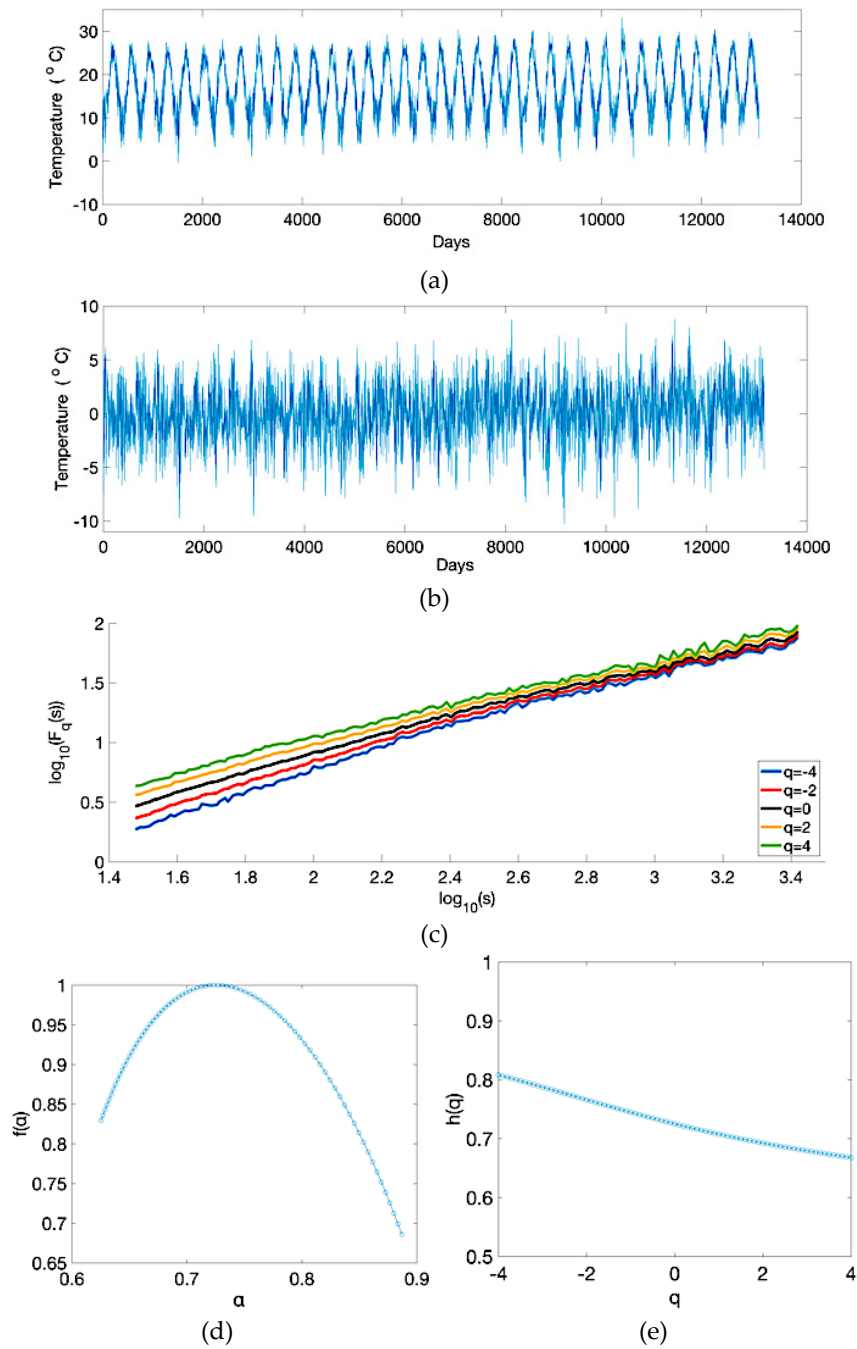


**Figure 2.** Original time series (a), deseasonalized time series (b), log-log plot of  $F_q(s)$  versus  $s$  (c), multifractal spectrum  $f(\alpha)$  versus  $\alpha$  for the nearest grid point to Athens (38.25° N, 24.00° E) (d) and generalized Hurst exponent  $h(q)$  versus  $q$  plot (e)

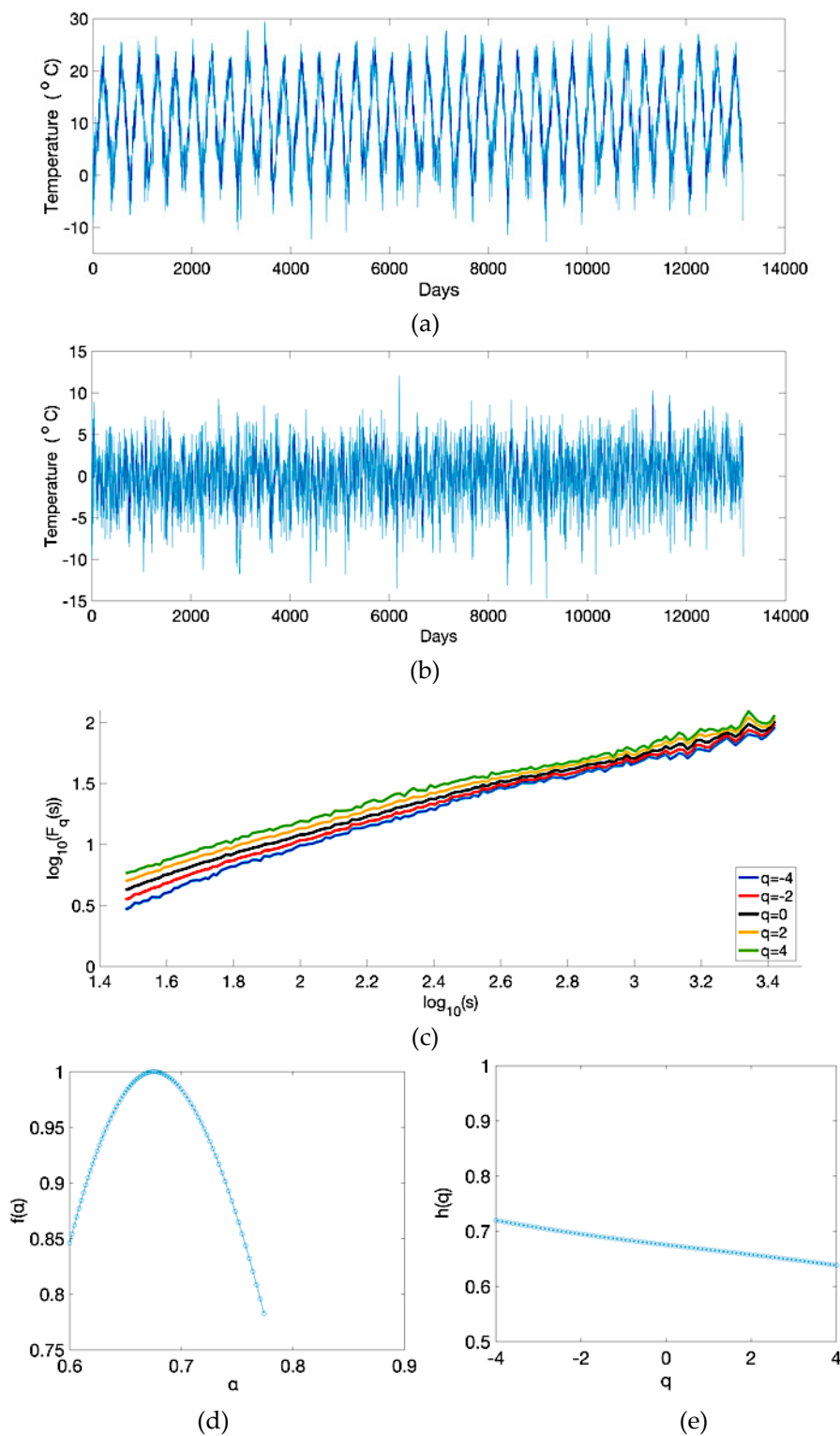


**Figure 3.** Original time series (a), deseasonalized time series (b), log-log plot of  $F_q(s)$  versus  $s$  (c), multifractal spectrum  $f(\alpha)$  versus  $\alpha$  for the nearest grid point to Kastoria ( $40.50^\circ$  N,  $21.00^\circ$  E) (d) and generalized Hurst exponent  $h(q)$  versus  $q$  plot (e).

These grid points represent geographic areas with different climatic conditions. The grid point that is close to Athens is a coastal point, located in southeastern central Greece, and therefore it is influenced by the sea. On the other hand, the second grid point, which is located in mountainous northwestern Greece, is not influenced by the sea characterized by a colder climate. This is clearly



reflected in Figures 2a and 3a, where below-zero temperatures are often observed, especially during winter in northwestern Greece. The scaling behavior is determined by the fluctuation functions  $F_q(s)$  (Figures 2c and 3c), which is similar in both grid points. The generalized Hurst exponent is greater than 0.5 in the two cases, revealing the fact that the temperature time series are long-range positively correlated. The most striking differences can be seen in the values of  $h(q)$ , which are greater for the point located near to Athens (Figures 2e and 3e). In addition to this, from Figures 2d and 3d, it is observed that the value of  $\alpha$  for which  $f(\alpha)$  is maximum is greater for the point located near to Athens. This fact can be attributed to the influence of the sea, which leads to a more persistent behavior (that is, greater scaling exponents) as will be stated in the next paragraph. Moreover, the spectrum of the mountainous area (Figure 3d) is narrower than the spectrum of Figure 2d. This can be attributed to the complex topography of the mountainous areas, which is the cause of local weather conditions that, in turn, make temperature fluctuations to be noisier; a time series that has a structure similar to white noise has a narrow spectrum [56,57].

It should be noted that  $F_q(s)$  is plotted for  $s$  ranging from  $10^{1.5}$  to  $10^{3.5}$  in days. In all cases, the form of  $F_q(s)$  plots is almost linear, and, for different  $q$  values, their distance is decreased when  $s$  increases. This is attributed to the fact that, for small segments (small  $s$  values), local periods with small fluctuations (negative  $q$ ) are easier to distinguish from periods with large fluctuations (positive  $q$ ). On the contrary, large segments include periods of both small and large fluctuations and therefore the differences in magnitude are cancelled [56]. This results in the behavior of  $F_q(s)$  for large segments being similar to monofractal time series (i.e., the  $F_q(s)$  for monofractal time series is independent of  $q$  and in that case the  $F_q(s)$  lines coincide). The multifractal character of the temperature time series is exhibited from the fact that the Hurst exponent is dependent on  $q$  (Figure 2d) and from the upside-down parabola form of the multifractal spectrum (Figure 2e). In more detail, in all cases  $h(q) > 0.5$ , and consequently the temperature time series are long-range positively correlated and therefore it is highly likely that an increase/decrease in temperature values will be followed by another increase/decrease.

In Figure 4, the log-log plots of  $F_2(s)$  versus  $s$  are illustrated for two representative grid points located over land (Land1: 39.75° N, 21.75° E, Land2: 37.50° N, 22.50° E) and for two points over sea (Sea1: 35.25° N, 27.75° E, Sea2: 36.75° N, 21.00° E). For each plot, a linear equation of the form  $y = ax + b$  is fitted, where  $a$  is the scaling exponent. It should be noted that, in all cases, high goodness-of-fit is achieved with coefficient of determination values greater than 99%. The estimated scaling exponents over sea are higher due to the influence of the higher seawater heat capacity, which leads to temperature time series with a higher degree of persistence. Furthermore, the lower  $F_2(s)$  values over sea can be attributed to the smaller temperature fluctuations.

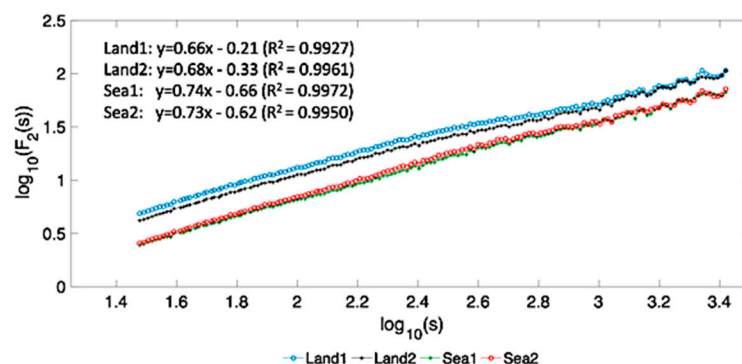


**Figure 4.** Log-log plots of  $F_2(s)$  for two grid points located over land (Land1: 39.75° N, 21.75° E, Land2: 37.50° N, 22.50° E) and for two points located over sea (Sea1: 35.25° N, 27.75° E, Sea2: 36.75° N, 21.00° E) along with the linear fit equations and the corresponding coefficient of determination  $R^2$  values.

The multifractal characteristics, deduced from the multifractal spectrum (i.e.,  $\alpha_{max} - \alpha_{min}$  width,  $\alpha_0$ , asymmetry parameter  $B$ , and truncation type), reveal important properties of the time series

multifractality and their value distributions are illustrated in Figure 5. The  $\alpha_0$  values range from 0.675 to 0.819 and, therefore, the dominant scaling exponent is greater than 0.5. In agreement with the  $h(q)$  findings, the dominant scaling behavior is persistent and positively correlated. The spectrum width values lie within the range of 0.380–0.650 and the asymmetry parameter values are in the range of  $-0.087$ – $0.698$ . The  $B$  distribution demonstrates that the majority of the asymmetry values are positive and, therefore, in general, the spectra are right-skewed. As suggested by [57], a right-skewed spectrum shows relatively strongly weighted high fractal exponents (with a ‘fine structure’). Additionally, the examination of the truncation type of the spectra shows that the majority of the spectra are left-truncated, which is also indicative that, in general, there is a dominance of high fractal exponents.

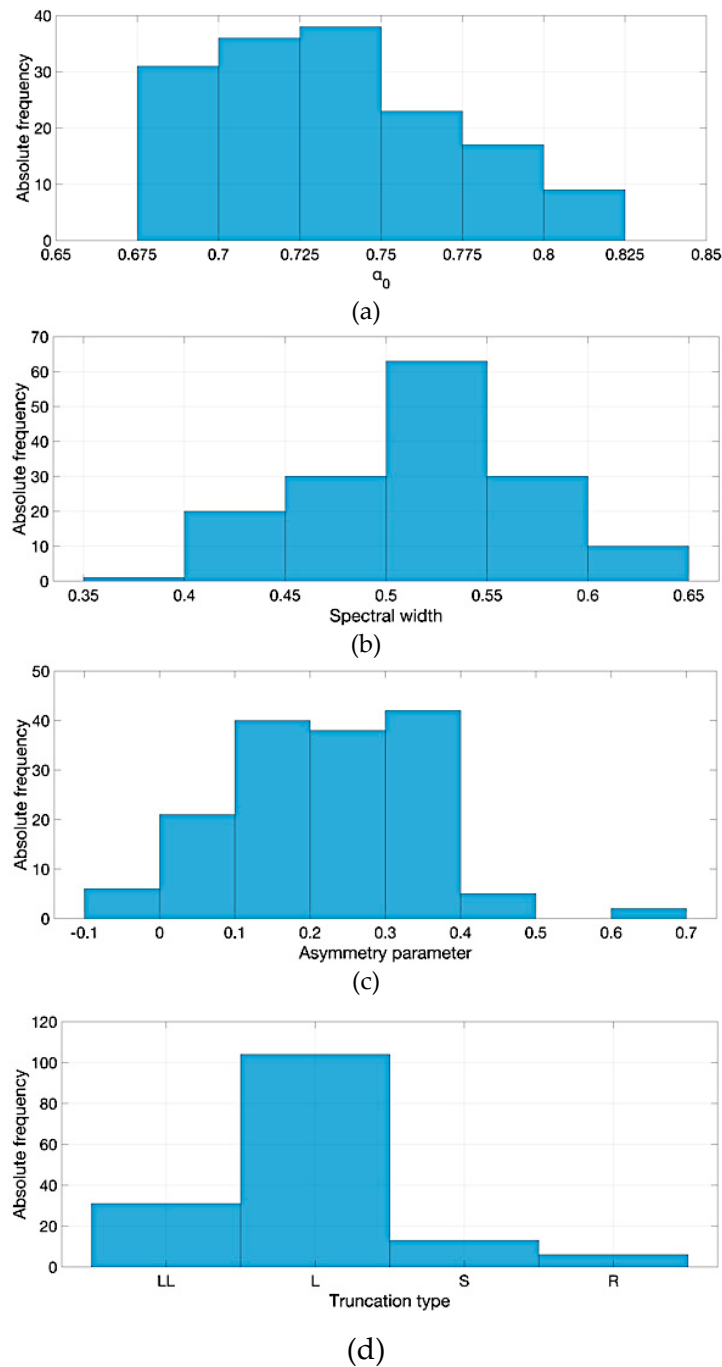


**Figure 5.** Multifractal spectral parameters distributions for  $\alpha_0$  (a), spectral width (b), asymmetry parameter (c), and truncation type (d).



The type of multifractality of the temperature time series is examined by shuffling the time series and applying the MF-DFA to the shuffled time series. The results revealed that the shuffled time series exhibit a very weak multifractality and, therefore, the multifractality is caused mainly by different long-range correlations for small and large fluctuations. A representative case is depicted in Figure 6. In the multifractal spectrum of the shuffled time series, the value of  $\alpha_0$  is very close to 0.5 and the spectrum width is clearly smaller than the corresponding width of the original time series.

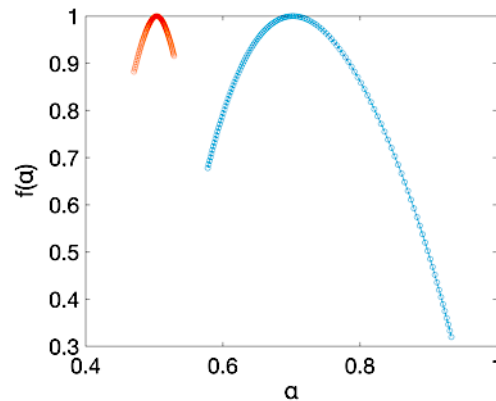


**Figure 6.** Multifractal spectra for the original (right) and for the shuffled (left) time series. The plots are for the closest to Thessaloniki grid point (40.50° N, 23.25° E).

#### 4.2. Multifractal Characteristics Spatial Distribution

The spatial distributions of the multifractal characteristics are illustrated in Figure 7. Regarding the  $\alpha_0$  spatial distribution (Figure 7a), the greater values are observed over marine areas, while lower values (darker color) dominate over land and, therefore, the time series exhibit a less persistent behavior over the continental areas of the domain. This finding could be attributed to the day-to-day variability of temperature, which is smaller over marine areas [59,60]. Over land, local weather conditions, such as katabatic winds, diabatic cooling or heating over ground, and the effect of elevation, lead to increased temperature variability. On the contrary, the greater heat capacity of seawater and the atmosphere–ocean interaction result in smaller changes in daily temperature. The same findings are also recognized in the spatial distribution of the Hurst exponent  $h(2)$  (Figure 7e). The spatial distribution of spectral width (Figure 7b) is very similar to that of  $\alpha_0$ . This can be attributed to the effect of complex terrain on local weather conditions, where temperature changes act as ‘noise’ to the smoother temperature changes caused by synoptic weather systems over land and to the effect of the sea over marine areas, where temperature changes exhibit a more persistent behavior.

The spatial distribution of the asymmetry parameter (Figure 7c) exhibits lower values over a part of continental Greece. This could be attributed to the fact that local weather parameters have a ‘noisy’ contribution to the multifractal spectrum, where the existence of low fractal exponents cancels out the right skewness caused by high fractal exponents. Additionally, the asymmetry parameter has, in general, higher values over the Aegean Sea than over other marine areas. This could be explained partially by the persistence of the Etesian winds [61] during summer, which affects accordingly the temperature field over the Aegean Sea. A similar situation is observed at the spatial distribution of truncation type (Figure 7d), where areas with lower values of asymmetry parameters appear to have a symmetrical or right-truncated spectrum.

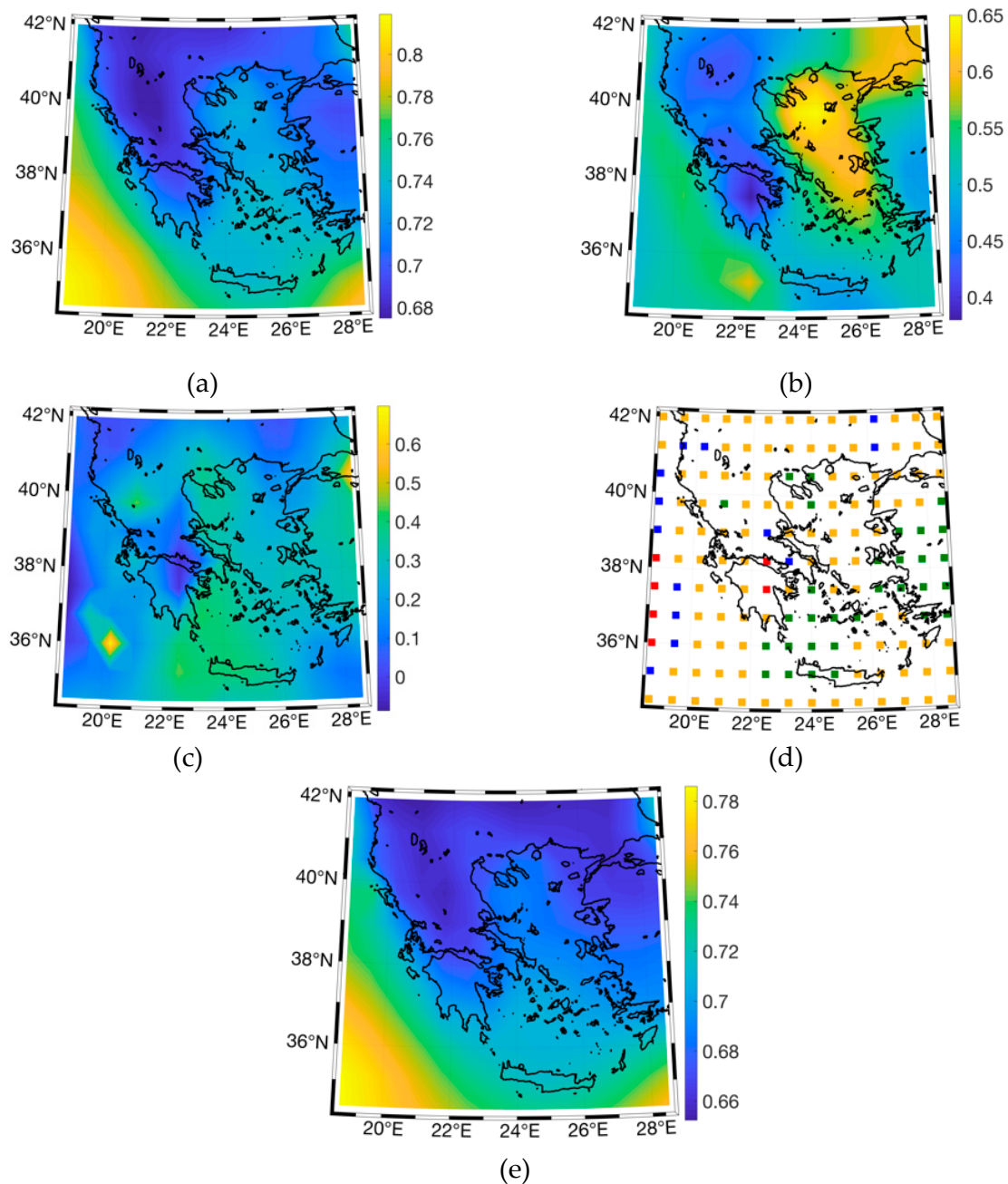


**Figure 7.** Spatial distribution of  $a_0$  (a), spectral width (b), asymmetry parameter (c), truncation type (d) where (LL: green squares, L: orange squares, S: blue squares, and R: red squares), and  $h(2)$  (e).

### 5. Discussion

An additional scope of this study is to compare the scaling behavior of the reanalysis temperature time series with the corresponding findings from observational records from 22 land-based meteorological stations presented in [49]. The multifractal spectral parameters from the observational records and those from their nearest reanalysis data grid points are illustrated in Table 1. For the reader’s convenience, the station names and the corresponding nearest grid points are also given in Table 1. In all cases, the  $a_0$  differences are small (below 10%) and, therefore, the scaling behavior is virtually the same in both cases. Regarding the spectral width and the asymmetry parameters, greater differences between the two datasets are observed, which could be attributed mainly to the method used in deriving the temperature time series.

**Table 1.** Spectral parameters’ values of observational (Obs) and ERA-Interim (ERA) time series for the closest to the station grid points.

Station	Nearest Point	$\alpha_0$		Spectral Width		Asymmetry Parameter	
		Obs	ERA	Obs	ERA	Obs	ERA
Alexandroupoli	40.50° N, 26.25° E	0.685	0.714	0.545	0.600	0.180	0.177
Andravida	38.25° N, 21.00° E	0.720	0.719	0.664	0.502	0.496	0.291
Elefsina	38.25° N, 23.25° E	0.708	0.705	0.629	0.441	0.416	0.086
Hellinikon	38.25° N, 24.00° E	0.719	0.725	0.659	0.532	0.399	0.344
Herakleio	35.25° N, 25.50° E	0.712	0.744	0.458	0.484	0.375	0.362
Kastoria	40.50° N, 21.00° E	0.713	0.675	0.479	0.421	0.038	0.252
Kerkira	39.75° N, 20.25° E	0.712	0.690	0.447	0.442	0.224	0.272
Kithira	36.00° N, 23.25° E	0.688	0.741	0.388	0.498	0.497	0.384
Kos	36.75° N, 27.00° E	0.747	0.737	0.511	0.549	0.037	0.270
Lamia	39.00° N, 22.50° E	0.718	0.689	0.500	0.446	0.478	0.066
Larisa	39.75° N, 22.50° E	0.684	0.693	0.659	0.466	0.685	0.105
Limnos	39.75° N, 25.50° E	0.725	0.724	0.566	0.620	0.255	0.218
Methoni	36.75° N, 21.75° E	0.734	0.737	0.548	0.497	0.396	0.283
Milos	36.75° N, 24.75° E	0.696	0.744	0.470	0.536	0.214	0.340
Mitilini	39.00° N, 26.25° E	0.715	0.717	0.532	0.580	0.269	0.259
Naxos	36.75° N, 25.50° E	0.775	0.744	0.677	0.553	0.305	0.297
Preveza	39.00° N, 21.00° E	0.720	0.695	0.727	0.426	0.577	0.087
Rodos	36.00° N, 27.75° E	0.730	0.756	0.437	0.523	0.097	0.161
Skiros	39.00° N, 24.75° E	0.703	0.731	0.544	0.615	0.409	0.271
Souda	35.25° N, 24.00° E	0.691	0.745	0.688	0.490	0.287	0.399
Thessaloniki	40.50° N, 23.25° E	0.717	0.702	0.463	0.521	0.299	0.377
Tripoli	37.50° N, 22.50° E	0.734	0.701	0.380	0.380	0.317	−0.029

More specifically,  $\alpha_0$  values for the observational data are of the order of 0.7, which verifies the long-range positively correlated behavior of the temperature time series. However, the dependence of  $\alpha_0$  on land–sea distribution, which is evident in the reanalysis data results, is not clearly observed in the results from observational records. The most persistent behavior for the observational records is observed at southeastern Greece and parts of coastal western Greece; these two areas have more stable climatic conditions in Greece [50]. The range of spectrum width values is almost the same for the observational and reanalysis data, but likewise to  $\alpha_0$ , the role of land–sea distribution is not clearly detected. In addition, the behavior of the shuffled observational and reanalysis data is the same, which means that the multifractality is mainly due to different long-range correlations for different magnitudes of fluctuations.

Regarding the asymmetry parameter and truncation type spatial distributions, the reanalysis data findings are in accordance with the observational records results (positive values dominate in the experimental domain). The close relationship between the asymmetry parameter and truncation type, though it is not straightforward, is verified by Table 2. In general, left-truncated spectra are related to higher asymmetry parameter values than right-truncated spectra. In the latter case, the values of the asymmetry parameter are negative.

**Table 2.** Range of asymmetry parameter values for each truncation type.

Truncation Type	Asymmetry Parameter
LL	0.288–0.450
L	0.033–0.698
S	0.029–0.341
R	−0.087–0.016

Another reason for the differences in multifractal spectrum characteristics between the observational and reanalysis time series is that the area of the study is evenly covered in the case of

ERA-Interim reanalysis by a grid of 154 points, whereas only 22 weather stations have been used for the observational data analysis, which are more sparsely and unevenly distributed.

## 6. Conclusions

The MF-DFA analysis of the ERA-Interim reanalysis temperature data revealed that the time series are long-range positively correlated. In particular, the spatial distribution of the  $\alpha_0$  parameter reveals a clear influence from the land/sea distribution. Lower  $\alpha_0$  values are observed over land, whereas higher values prevail over marine areas, where temperature exhibits a more persistent behavior. This could be attributed to the higher seawater heat capacity. Regarding the spectral width, it is observed that higher values are found over marine areas, whereas lower values dominate over land and, thus, temperature time series at marine areas exhibit a higher degree of multifractality compared to continental areas. This finding could be attributed to the greater temperature variations over land. Such behavior is closer to that of white noise, which has a narrow spectrum [56]. On the other hand, the behavior is more persistent over sea and, therefore, temperature time series over marine areas appear to have a greater number of spectral components with higher Hölder exponent values. Moreover, it was deduced from the shuffled data spectra that the multifractal spectrum width is significantly smaller (of the order of 0.2) compared to that of the original data. This means that the multifractality is mainly due to different long-range correlations for different magnitudes of fluctuations. The values of the asymmetry parameter are positive in almost all areas (right-skewed spectra), which is indicative of the presence of strongly weighted high fractal exponents [57]. This is also confirmed from the dominance of left-truncated spectra. Future work will be focused on examining the multifractal characteristics of additional climatic parameters from experimental and reanalysis datasets for using the results in applied climatology.

**Author Contributions:** Conceptualization, K.P., N.K., C.G.T. and D.D.; Methodology, K.P., N.K., C.G.T. and D.D.; Software, K.P., N.K., C.G.T., D.D. and I.K.; Validation, K.P., N.K., C.G.T., D.D. and I.K.; Formal Analysis, K.P., N.K., C.G.T., D.D. and I.K.; Investigation, K.P., N.K., C.G.T. and D.D.; Data Curation, K.P., N.K., C.G.T., D.D. and I.K.; Writing—original draft preparation, K.P., N.K., C.G.T., D.D. and I.K.; Writing—review and editing, K.P., N.K., C.G.T., D.D. and I.K.; Visualization, K.P., N.K. and I.K.; Visualization, K.P., N.K. and I.K.; Supervision, K.P., C.G.T. and D.D.

**Funding:** This research received no external funding.

**Conflicts of Interest:** The authors declare no conflicts of interest.

## References

1. Mandelbrot, B.B. *Fractals: Form, Chance and Dimension*; Freeman: San Francisco, CA, USA, 1977.
2. Mandelbrot, B.B. *The Fractal Geometry of Nature*; Freeman: San Francisco, CA, USA, 1982.
3. Feder, J. *Fractals*; Plenum: New York, NY, USA, 1988.
4. Barnsley, M.F. *Fractals Everywhere*; Academic Press: San Diego, CA, USA, 1993.
5. Mandelbrot, B.B. *Multifractals and 1/f Noise: Wild Self-Affinity in Physics*; Springer: Berlin, Germany, 1999.
6. Kandelhardt, J.W. Fractal and Multifractal Time Series. In *Mathematics of Complexity and Dynamical Systems*; Meyers, R.A., Ed.; Springer: New York, NY, USA, 2011; pp. 463–487.
7. Peng, C.K.; Buldyrev, S.V.; Havlin, S.; Simons, M.; Stanley, H.E.; Goldberger, A.L. Mosaic organization of DNA nucleotides. *Phys. Rev. E* **1994**, *49*, 1685–1689. [[CrossRef](#)]
8. Kandelhardt, J.W.; Koscielny-Bunde, E.; Rego, H.A.H.; Havlin, S.; Bunde, A. Detecting long-range correlations with detrended fluctuation analysis. *Physica A* **2001**, *295*, 441–454. [[CrossRef](#)]
9. Liu, Y.; Cizeau, P.; Meyer, M.; Peng, C.K.; Stanley, H.E. Correlations in economic time series. *Physica A* **1997**, *245*, 437–440. [[CrossRef](#)]
10. Di Matteo, T.; Aste, T.; Dacorogna, M.M. Scaling behaviors in differently developed markets. *Physica A* **2003**, *324*, 183–188. [[CrossRef](#)]
11. Barbi, M.; Chillemi, S.; Di Garbo, A.; Balocchi, R.; Carpeggiani, C.; Emdin, M.; Michelassi, C.; Santarcangelo, E. Predictability and nonlinearity of the heart rhythm. *Chaos Soliton Fract.* **1998**, *9*, 507–515. [[CrossRef](#)]

12. Buldyrev, S.V.; Dokholyan, N.V.; Goldberger, A.L.; Havlin, S.; Peng, C.K.; Stanley, H.E.; Viswanathan, G.M. Analysis of DNA sequences using methods of statistical physics. *Physica A* **1998**, *249*, 430–438. [[CrossRef](#)]
13. Gao, J.; Hu, J.; Mao, X.; Perc, M. Culturomics meets random fractal theory: Insights into long-range correlations of social and natural phenomena over the past two centuries. *J. Royal Soc. Interface* **2012**, *9*, 1956–1964. [[CrossRef](#)]
14. Varotsos, C.A.; Melnikova, I.; Efstathiou, M.N.; Tzani, C. 1/f noise in the UV solar spectral irradiance. *Theor. Appl. Climatol.* **2013**, *111*, 641–648. [[CrossRef](#)]
15. Chattopadhyay, G.; Chattopadhyay, S. Study on statistical aspects of monthly sunspot number time series and its long-range correlation through detrended fluctuation analysis. *Indian J. Phys.* **2014**, *88*, 1135–1140. [[CrossRef](#)]
16. Holton, J.R. *An introduction to Dynamic Meteorology*, 4th ed.; Elsevier Academic Press: Cambridge, MA, USA, 2004.
17. Koscielny-Bunde, E.; Bunde, A.; Havlin, S.; Goldreich, Y. Analysis of daily temperature fluctuations. *Physica A* **1996**, *231*, 393–396. [[CrossRef](#)]
18. Eichner, J.F.; Koscielny-Bunde, E.; Bunde, A.; Havlin, S.; Schellnhuber, H.J. Power-law persistence and trends in the atmosphere: A detailed study of long temperature records. *Phys. Rev. E* **2003**, *68*, 046133. [[CrossRef](#)] [[PubMed](#)]
19. Bartos, I.; Janosi, I.M. Nonlinear correlations of daily temperature records over land. *Nonlinear Proc. Geophys.* **2006**, *13*, 571–576. [[CrossRef](#)]
20. Orun, M.; Koçak, K. Application of detrended fluctuation analysis to temperature data from Turkey. *Int. J. Climatol.* **2009**, *29*, 2130–2136. [[CrossRef](#)]
21. Yuan, N.; Fu, Z.; Mao, J. Different scaling behaviors in daily temperature records over China. *Physica A* **2010**, *389*, 4087–4095. [[CrossRef](#)]
22. Kalamaras, N.; Philippopoulos, K.; Deligiorgi, D. Scaling Properties of Meteorological Time Series Using Detrended Fluctuation Analysis. In *Perspectives on Atmospheric sciences, Proceedings of the 13th International Conference of Meteorology, Climatology and Atmospheric Physics, Thessaloniki, Greece, 19–21 September 2016*; Karacostas, T.S., Bais, A.F., Nastos, P.T., Eds.; Springer Atmospheric Physics; Springer International Publishing: Cham, Switzerland, 2016; pp. 545–550.
23. Podobnik, B.; Ivanov, P.C.; Jazbinsek, V.; Trontelj, Z.; Stanley, H.E.; Grosse, I. Power-law correlated processes with asymmetric distributions. *Phys. Rev. E* **2005**, *71*, 025104. [[CrossRef](#)] [[PubMed](#)]
24. Lin, G.; Chen, X.; Fu, Z. Temporal–spatial diversities of long-range correlation for relative humidity over China. *Physica A* **2007**, *383*, 585–594. [[CrossRef](#)]
25. Jiang, L.; Zhao, L.; Zhao, Z. On the Difference of Scaling Properties for Temperature and Precipitation over China. *Adv. Meteorol. Hindawi* **2017**, *2017*. [[CrossRef](#)]
26. He, W.; Zhao, S.; Liu, Q.; Jiang, Y.; Deng, B. Long-range correlation in the drought and flood index from 1470 to 2000 in eastern China. *Int. J. Climatol.* **2016**, *36*, 1676–1685. [[CrossRef](#)]
27. Varotsos, C.A.; Tzani, C. A new tool for the study of the ozone hole dynamics over Antarctica. *Atmos. Environ.* **2012**, *47*, 428–434. [[CrossRef](#)]
28. Varotsos, C.A.; Milinevsky, G.; Grytsai, A.; Efstathiou, M.; Tzani, C. Scaling effect in planetary waves over Antarctica. *Int. J. Remote Sens.* **2008**, *29*, 2697–2704. [[CrossRef](#)]
29. Varotsos, C.; Efstathiou, M.; Tzani, C.; Deligiorgi, D. On the limits of the air pollution predictability: the case of the surface ozone at Athens, Greece. *Environ. Sci. Pollut. Res.* **2012**, *19*, 295–300. [[CrossRef](#)] [[PubMed](#)]
30. Varotsos, C.; Tzani, C.; Efstathiou, M.; Deligiorgi, D. Tempting long-memory in the historic surface ozone concentrations at Athens, Greece. *Atmos. Pollut. Res.* **2015**, *6*, 1055–1057. [[CrossRef](#)]
31. Varotsos, C.A.; Lovejoy, S.; Sarlis, N.V.; Tzani, C.G.; Efstathiou, M.N. On the scaling of the solar incident flux. *Atmos. Chem. Phys.* **2015**, *15*, 7301–7306. [[CrossRef](#)]
32. Lovejoy, S. A voyage through scales, a missing quadrillion and why the climate is not what you expect. *Clim. Dyn.* **2015**, *44*, 3187–3210. [[CrossRef](#)]
33. Caldeira, R.; Fernandez, I.; Pacheco, J.M. On NAO's predictability through the DFA method. *Meteorol. Atmos. Phys.* **2007**, *96*, 221–227. [[CrossRef](#)]
34. Kandelhardt, J.W.; Zschiegner, S.A.; Koscielny-Bunde, E.; Havlin, S.; Bunde, A.; Stanley, H.E. Multifractal detrended fluctuation analysis of nonstationary time series. *Physica A* **2002**, *316*, 87–114. [[CrossRef](#)]



35. Lovejoy, S.; Schertzer, D. *The Weather and Climate Emergent Laws and Multifractal Cascades*; Cambridge University Press: New York, NY, USA, 2013.
36. Kalamaras, N.; Philippopoulos, K.; Deligiorgi, D.; Tzanis, C.G.; Karvounis, G. Multifractal scaling properties of daily air temperature time series. *Chaos Solitons Fractals*. **2017**, *98*, 38–43. [[CrossRef](#)]
37. Svensson, C.; Olsson, J.; Berndtsson, R. Multifractal properties of daily rainfall in two different climates. *Water Resour. Res.* **1996**, *332*, 2463–2472. [[CrossRef](#)]
38. Du, H.; Wu, Z.; Zong, S.; Meng, X.; Wang, L. Assessing the characteristics of extreme precipitation over northeast China using the multifractal detrended fluctuation analysis. *J. Geophys. Res. Atmos* **2013**, *118*, 6165–6174. [[CrossRef](#)]
39. Shao, Z.-G.; Ditlevsen, P. Contrasting scaling properties of interglacial and glacial climates. *Nat. Commun.* **2016**, *7*, 10951. [[CrossRef](#)]
40. Zhang, X.; Zhang, G.; Qiu, L.; Zhang, B.; Sun, Y.; Gui, Z.; Zhang, Q. A Modified Multifractal Detrended Fluctuation Analysis (MFDFA) Approach for Multifractal Analysis of Precipitation in Dongting Lake Basin, China. *Water* **2019**, *11*, 891. [[CrossRef](#)]
41. Kavasseri, R.G.; Nagarajan, R. A multifractal description of wind speed records. *Chaos Soliton Fract.* **2005**, *24*, 165–173. [[CrossRef](#)]
42. Feng, T.; Fu, Z.; Deng, X.; Mao, J. A brief description to different multi-fractal behaviors of daily wind speed records over China. *Phys. Lett. A* **2009**, *373*, 4134–4141. [[CrossRef](#)]
43. Laib, M.; Telesca, L.; Kanevski, M. Long-range fluctuations and multifractality in connectivity density time series of a wind speed monitoring network. *Chaos* **2018**, *28*, 033108. [[CrossRef](#)] [[PubMed](#)]
44. Pedron, I.T. Correlation and multifractality in climatological time series. *J. Phys. Conf. Ser.* **2010**, *246*, 012034. [[CrossRef](#)]
45. Baranowski, P.; Krzyszczak, J.; Slawinski, C.; Hoffmann, H.; Kozyra, J.; Nieróbca, A.; Siwek, K.; Gluza, A. Multifractal analysis of meteorological time series to assess climate impacts. *Clim. Res.* **2015**, *65*, 39–52. [[CrossRef](#)]
46. Hoffmann, H.; Baranowski, P.; Krzyszczak, J.; Zubik, M.; Sławiński, C.; Gaiser, T.; Ewert, F. Temporal properties of spatially aggregated meteorological time series. *Agric. Forest Meteorol.* **2017**, *234–235*, 247–257.
47. Krzyszczak, J.; Baranowski, P.; Zubik, M.; Hoffmann, H. Temporal scale influence on multifractal properties of agro-meteorological time series. *Agric. Forest Meteorol.* **2017**, *239*, 223–235. [[CrossRef](#)]
48. Xue, Y.; Pan, W.; Lu, W.; He, H. Multifractal nature of particulate matters (PMs) in Hong Kong urban air. *Sci. Total Environ.* **2015**, *532*, 744–751. [[CrossRef](#)]
49. Kalamaras, N.; Tzanis, C.G.; Deligiorgi, D.; Philippopoulos, K.; Koutsogiannis, I. Distribution of air temperature multifractal characteristics over Greece. *Atmosphere* **2019**, *10*, 45. [[CrossRef](#)]
50. Mariolopoulos, E.G. *The Climate of Greece*; A.A. Papaspyrou Press: Athens, Greece, 1938. (In Greek)
51. Karras, G. Climatic Classification of Greece According to Thornthwaite. Ph.D. Thesis, National and Kapodistrian University of Athens, Athens, Greece, 1973. (In Greek).
52. Feidas, H.; Makrogiannis, T.; Bora-Senta, E. Trend analysis of air temperature time series in Greece and their relationship with circulation using surface and satellite data: 1955–2001. *Theor. Appl. Climatol.* **2004**, *79*, 185–208. [[CrossRef](#)]
53. Dee, D.P.; Uppala, S.M.; Simmons, A.J.; Berrisford, P.; Poli, P.; Kobayashi, S.; Andrae, U.; Balmaseda, M.A.; Balsamo, G.; Bauer, P.; et al. The ERA-Interim reanalysis: Configuration and performance of the data assimilation system. *Q. J. Royal Meteorol. Soc.* **2011**, *137*, 553–597. [[CrossRef](#)]
54. Berrisford, P.; Dee, D.; Poli, P.; Brugge, R.; Fielding, K.; Fuentes, M.; Kallberg, P.; Kobayashi, S.; Uppala, S.; Simmons, A. *The ERA-Interim Archive*, version 2.0; ERA Report Series; ECMWF Publications: Reading, UK, 2011.
55. Bishop, S.M.; Yarham, S.I.; Navapurkar, V.U.; Menon, D.K.; Ercole, A. Multifractal analysis of hemodynamic behavior: Intraoperative instability and its pharmacological manipulation. *Anesthesiology* **2012**, *117*, 810–821. [[CrossRef](#)] [[PubMed](#)]
56. Ihlen, E.A.F. Introduction to multifractal detrended fluctuation analysis in Matlab. *Front. Physiol.* **2012**, *3*, 141. [[CrossRef](#)] [[PubMed](#)]
57. Shimizu, Y.; Thurner, K.; Ehrenberger, K. Multifractal spectra as a measure of complexity in human posture. *Fractals* **2002**, *10*, 103–116. [[CrossRef](#)]



58. Burgueno, A.; Lana, X.; Serra, C.; Martinez, M.D. Daily extreme temperature multifractals in Catalonia (NE Spain). *Phys. Lett. A* **2014**, *378*, 874–885. [[CrossRef](#)]
59. Bountas, N.; Boboti, N.; Feloni, E.; Zeikos, L.; Markonis, Y.; Tegos, A.; Mamassis, N.; Koutsoyiannis, D. Temperature variability over Greece: Links between space and time. In Proceedings of the 5th EGU Leonardo Conference, Kos Island, Greece, 17–19 October 2013.
60. Stathopoulos, V.; Fotiadi, A.; Houssos, E.E.; Hatzianastassiou, N.; Vardavas, I. Day to Day Variability of Air Temperature over Greece for the Period 1957–2002. In *Advances in Meteorology, Climatology and Atmospheric Physics*; Springer Atmospheric Sciences; Springer: Berlin/Heidelberg, Germany, 2012; pp. 737–742.
61. Metaxas, D.A. The interannual variability of the Etesian frequency as a response of atmospheric circulation anomalies. *Bull Hell Meteorol. Soc.* **1977**, *2*, 30–40.



© 2019 by the authors. Licensee MDPI, Basel, Switzerland. This article is an open access article distributed under the terms and conditions of the Creative Commons Attribution (CC BY) license (<http://creativecommons.org/licenses/by/4.0/>).